Fuel 272 (2020) 117658

Contents lists available at ScienceDirect

Fuel

journal homepage: www.elsevier.com/locate/fuel

Computational analysis of premixed methane-air flame interacting with a solid wall or a hydrogen porous wall

Prashant S. Salimath[a], Ivar S. Ertesvåg[a,*], Andrea Gruber[a,b]

[a] Department of Energy and Process Engineering, NTNU Norwegian University of Science and Technology, Kolbjørn Hejes vei 1b, NO-7491 Trondheim, Norway
[b] SINTEF Energy Research, Trondheim, Norway

ARTICLE INFO

Keywords:
Impermeable wall
Permeable wall
S3D code
Head on quenching
Smooke and Giovangigli mechanism
DRM22 mechanism

ABSTRACT

The process of flame-wall interaction for premixed methane-air flames is investigated by direct numerical simulation. The flames propagate towards an isothermal, chemically inert surface, consisting of either a solid impermeable wall (IW) material or a hydrogen-permeable wall (PW) material. With the PW, hydrogen seeps into the domain and participate as a secondary, non-premixed fuel. The skeletal methane-air chemical reaction kinetics mechanisms of Smooke and Giovangigli and DRM22 are used with the S3D code to study the major reactions controlling the flame-wall interactions (FWI). Initially, results of said mechanisms are compared to the complete GRI 3.0 scheme. The configurations are investigated for two temperatures, 600 K and 750 K, of the wall and the unburnt gas, and for initial equivalence ratios of 0.5, 1.0 and 1.5. Results for IW are similar to previous FWI studies. The flame quenches at the wall, with maximum heat release and wall heat flux occurring close to the quenching instance. For the PW cases, the flame quenches before reaching the wall. This is explained by the mutual effects of convective heat transfer away from the wall and flame due to permeation, a high concentration of hydrogen and high local fuel-to-oxidizer ratio, reduced temperature and reduced reaction heat release. The quenching definition and flame position are based on OH radicals concentration. The observed maximum wall heat flux is much lower than for IW, and occurs some time after quenching. A discussion about the quenching process indicates that a definition based on maximum wall heat flux is inappropriate.

1. Introduction

Recent efforts towards low-emission and sustainable solutions for power and transport, paired with increasingly high power densities, necessarily imply that industrial combustion devices will be subject to more restrictive emissions and efficiency standards and, simultaneously, to intense reaction taking place closer to the combustion chamber walls. Large efficiency losses and pollutants formation in combustion devices take place in flame-wall interactions (FWI) that occur when the flame is quenched in the immediate vicinity of a solid surface [1,2]. However, in spite of their practical relevance, detailed physical insights about FWI processes have been difficult to extract from laboratory experiments, due to important challenges in performing accurate near-wall measurements. In this context, accurate state-of-the-art direct numerical simulation (DNS) remains an important tool in fundamental investigations of FWI processes [3–5].

The premixed FWI process is described as a freely propagating flame moving towards a (relatively) cold wall such that the flame quenches in the near-wall region due to thermal loss from the reaction zone to the wall. Accurate estimation of the quenching distance is important as it determines the unburnt layer subject to strong near-wall thermal gradients in energy conversion devices such as gas turbines and reciprocating engines. The present trend in engine downsizing increases the surface to volume ratio, with profound effects on near-wall combustion and pollutants formation. Previous numerical and experimental work on premixed FWI have investigated different parameters such as wall temperature, equivalence ratio, constant volume/pressure chambers and surface reactivity for hydrocarbon fuels [6–16] and for hydrogen [17–19,3,20]. In a comprehensive review, Dreizler and Böhm [2] summarized recent advancement and gave a detailed discussion on FWI, including methods for accurate quenching distance determination based on laser diagnostics and direct numerical simulations.

Typical numerical investigations of FWI phenomena are performed in canonical configuration setups of 1-dimensional head-on quenching (HOQ) and 2-d side-wall quenching. Transient 1-d HOQ is considered as an extreme case of FWI, with zero flame stretch and large thermal losses to the wall. Quenching distance, wall thermal transfer and exhaust composition are key parameters of 1-d FWI. These parameters depend

* Corresponding author.
E-mail addresses: Prashant.Salimath@ntnu.no (P.S. Salimath), Ivar.S.Ertesvag@ntnu.no (I.S. Ertesvåg), Andrea.Gruber@sintef.no (A. Gruber).

https://doi.org/10.1016/j.fuel.2020.117658
Received 8 December 2019; Received in revised form 12 March 2020; Accepted 17 March 2020

Nomenclature

Abbreviations

IW	Impermeable wall
PW	Permeable wall

Greek symbols

δ_L^0	Flame thickness, m
δ_L	Characteristic flame thickness, m
$\dot{\omega}$	Overall reaction heat release rate, W/m^3
$\dot{\omega}_k$	Molar production rate of species k, kg/(m^{3}s)
λ	Thermal conductivity of the gaseous mixture, W/(mK)
Φ	Heat flux, W/m^2
ϕ	Equivalence ratio, –
ρ	Density, kg/m^3

Latin symbols

Pe	Peclet number based on location of $\dot{\omega}_{max}$, –
Pe_F	Peclet number based on location of $-\dot{\omega}_{F,max}$, –
Pe_{OH^*}	Peclet number based on location of maximum OH gradient, –
C_p	Specific heat at constant pressure, J/(kgK)
D	Mass diffusivity, m^2/s
F_k	Mass flux of species k, kg/(m^{2}s)
L	Length of domain, m
M	Number of nodes within flame thickness at quenching, –
n	Pressure exponent of membrane, –
p	Pressure, Pa
q_l^0	Flame power, W/m^2
S_L^0	Laminar flame speed, m s^{-1}
T	Temperature, K
t	Time, s
u	Velocity, m s^{-1}
W_k	Molar mass of species k, kg/kmol
x	Spatial coordinate, m
y	Wall-flame distance, m
Y_k	Mass fraction of species k, –

Superscripts

f	Feed side
p	Permeate side

Subscripts

′	Non-dimensional values
*	Non-dimensional values
b	Burnt mixture
F	Fuel
max	Maximum value
mix	Mixture average
Q	Quenching
u	Unburnt mixture
w	Wall
k	Species index

on stoichiometry, wall and unburnt-gas temperatures and pressure. A higher pressure leads to decrease of quenching distance, while the FWI time remains unchanged [21]. In simulations using detailed chemical mechanisms for 1-d HOQ of laminar flames at constant pressure and stoichiometric conditions, increased wall temperature led to a significant increase of the wall thermal flux for methane [15,10], n-heptane [12] and iso-octane [7] mixtures with air.

State-of-the-art numerical simulations of FWI have typically employed detailed chemical mechanisms. Single-step and simplified chemical models showed good results of wall heat flux compared to experimental results for lower wall temperatures, around 300 K, for different equivalence ratios [22,14,16]. However, they failed for higher wall temperatures due to presence of low-activation radical recombination reactions near the wall [14]. When detailed chemical mechanisms were included, good FWI results in comparison to experimental data were achieved for wall temperatures above 400 K [10]. For 1-d HOQ configurations for both methane and hydrogen flames at elevated wall temperatures, exothermic radical recombination reactions and intermediate species contributed to large heat release at the wall during quenching [10,3,17]. Recently, complex chemistry models were used for acoustics due to flame annihilation in FWI. In the case of noise generation in 1-d HOQ at a wall of temperature 300 K, simple chemistry led to a faster extinction process and overestimating of pressure peaks during quenching compared to the detailed chemistry [23].

FWI involving hydrocarbon fuels for impermeable, inert-wall configurations showed inverse proportional relationships of normalized wall heat flux and flame quenching distance (i.e. quenching Peclet number). Boust et al. [11] developed modelling relationships between quenching distance and wall heat flux in 1-d HOQ for methane flames. These relationships do not hold true for hydrogen flames, as higher wall fluxes are observed with flame diffusing faster and reaching closer to the wall [17].

Recently, renewed interest in hydrogen selective membranes, in the context of carbon capture and storage (CCS) applications, has raised the issue of flame-wall interactions in the presence of a porous, permeable wall that can act as a source of hydrogen fuel. In two previous studies the present authors presented numerical investigations on the effects of

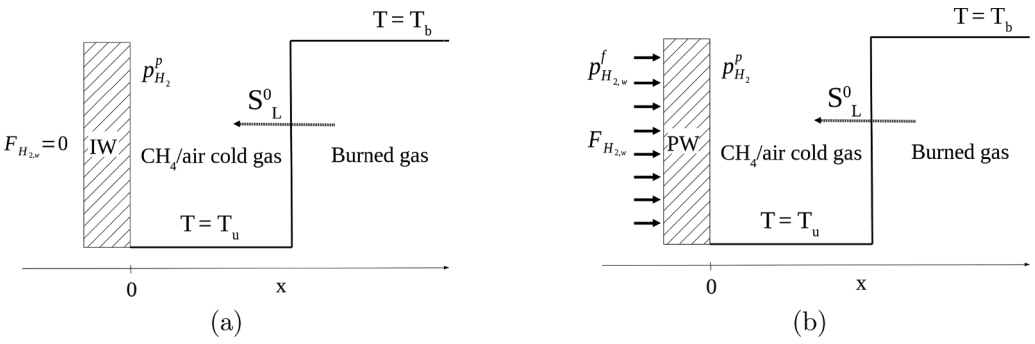

Fig. 1. Head-on quenching configurations of (a) Impermeable wall (IW) and (b) Permeable wall (PW) with hydrogen flux.

Table 1
Chemical mechanism by Smooke and Giovangigli [35] with rate coefficients $k_f = AT^{\beta}\exp(-E_0/RT)$.

No.	Reaction	A	β	E_0
R1	$H + O_2 \rightarrow OH + O$	2.00E+14	0.0	16800.0
R2	$O + H_2 \rightarrow OH + H$	1.80E+10	1.0	8826.0
R3	$H_2 + OH \rightarrow H_2O + H$	1.17E+09	1.30	3626.0
R4	$OH + OH \rightarrow O + H_2O$	6.00E+08	1.300	0.0
R5	$H + O_2 + M \rightarrow HO_2 + M$	2.30E+18	−0.80	0.0
R6	$H + HO_2 \rightarrow OH + OH$	1.50E+14	0.000	1900.0
R7	$H + HO_2 \rightarrow H_2 + O_2$	2.50E+13	0.0	700.0
R8	$OH + HO_2 \rightarrow H_2O + O_2$	2.00E+13	0.0	1000.0
R9	$CO + OH \rightarrow CO_2 + H$	1.51E+07	1.30	−758.0
R10	$CH_4 + (M) \rightarrow CH_3 + H + (M)$	2.30E+38	−7.0	114363.0
R11	$CH_4 + H \rightarrow CH_3 + H_2$	2.20E+04	3.0	8750.0
R12	$CH_4 + OH \rightarrow CH_3 + H_2O$	1.60E+06	2.10	2460.0
R13	$CH_3 + O \rightarrow CH_2O + H$	6.80E+13	0.0	0.0
R14	$CH_2O + H \rightarrow HCO + H_2$	2.50E+14	0.0	10500.0
R15	$CH_2O + OH \rightarrow HCO + H_2O$	3.00E+13	0.0	167.0
R16	$HCO + H \rightarrow CO + H_2$	4.00E+13	0.0	0.0
R17	$HCO + M \rightarrow CO + H + M$	1.60E+14	0.0	14700.0
R18	$CH_3 + O_2 \rightarrow CH_3O + O$	7.00E+12	0.0	25652.0
R19	$CH_3O + H \rightarrow CH_2O + H_2$	2.00E+13	0.0	0.0
R20	$CH_3O + M \rightarrow CH_2O + H + M$	2.40E+13	0.0	28812.0
R21	$HO_2 + HO_2 \rightarrow H_2O_2 + O_2$	2.00E+12	0.0	0.0
R22	$H_2O_2 + M \rightarrow 2OH + M$	1.30E+17	0.0	45500.0
R23	$H_2O_2 + OH \rightarrow H_2O + HO_2$	1.00E+13	0.0	1800.0
R24	$OH + H + M \rightarrow H_2O + M$	2.20E+22	−2.0	0.0
R25	$H + H + M \rightarrow H_2 + M$	1.80E+18	−1.0	0.0

an H_2 flux through a permeable wall into an H_2-air mixture and influence on the FWI heat fluxes: Gruber et al. [4] presented 1-d and 2-d FWI results for a high pressure of 10 atm at the permeate side and showed that a strong feedback mechanism exists between the permeating hydrogen flux and the flame. Salimath et al. [5] extended the study on the 1-d solid-wall and permeable-wall configurations and presented FWI results for different feed pressures, dilution with N_2 (inert) and H_2O (participating) and different wall temperatures. Furthermore, a recent experimental study has investigated the effects on premixed flame shape and stabilization of a novel approach for spatially distributed hydrogen injection through a porous steel surface integrated in the burner design [24].

Fig. 1 illustrates schematically the 1-d case of a planar flame front propagating through initially premixed methane-air and impinging upon a solid wall. This flame quenching process is shown for an impermeable wall (IW) or solid wall and a fuel-permeable wall (PW). In the PW case, high pressure at the feed side supplies H_2 as a secondary fuel into the domain. Hence, the flame becomes partially premixed on the permeate side.

The present study is an investigation of the configuration with methane-air mixtures and a selective H_2 porous wall at wall temperatures of 600 and 750 K. The hydrogen flux through the membrane influences the near-wall chemistry and wall heat transfer. We will investigate detailed FWI characteristics and influence of hydrogen influx on heat release rates near the wall for lean, stoichiometric and rich methane-air mixtures. The contributions of individual elementary reactions will be studied more in detail. This study aims at gaining understanding of near-wall chemistry and influence of hydrogen permeability in hardware components on quenching wall heat fluxes. The permeating secondary fuel can alter the local chemistry for a given mixture. The practical arrangement and implementation of permeability of H_2 fuel was outside the scope of this study, and no effort was made to show experimental setup of permeability of wall.

In the following, Section 2 describes the code, numerical setup, submodels and boundary conditions, and relevant quantities are defined. The flame-wall interaction results are presented in Section 3 and discussed in Section 4. Finally, conclusions are presented.

2. Numerical setup and submodels

2.1. Code, numerics and thermo-fluid models

The massively parallel DNS code, S3D, developed at Sandia National Laboratories [25], was used here for the 1-d FWI studies. The code handles inter-process communication in parallel execution through Message Passing Interface (MPI) [26]. It has been ported to different architectures for a variety of case studies [27,3,28–32]. It solves the conservative form of Navier-Stokes equations on structured, Cartesian grids in 1–3 spatial directions.

The numerical solver of the code employs a high order, non-dissipative central difference scheme. A spatial tenth-order explicit filter is employed at every 10 iterations to remove any spurious high frequency noise in the simulations resulting from aliasing errors and odd-even decoupling. An eight-order explicit central difference scheme is used within the computational domain, while a third order scheme (one sided stencils) at boundaries. A six-stage fourth-order explicit Runge-Kutta method is used in time [33].

Details of the governing equations and constitutive relationships, such as ideal gas equation of state, models for reaction rates, molecular transport and thermodynamic properties were described by Chen et al. [25] and hence, are only briefly mentioned here. The Soret effect (thermo-diffusion) and pressure diffusion were included, whereas the Dufour effect was not implemented in the code [25]. Body-force effects (gravity) and radiation heat transfer were neglected, following several previous premixed-flame studies of methane [14,16,23,10,34] and hydrogen flames [17,12,18,4]. The walls were assumed as chemically inert, with no adsorption or catalytic effects.

2.2. Chemical mechanisms

Chemistry was modelled by three different mechanisms: Reduced chemistry of methane-air combustion was described by Smooke and Giovangigli [35] (SG in the following). This 25-step mechanism includes 16 species: H_2, H, O, O_2, OH, H_2O, HO_2, CH_4, CO, CO_2, H_2O_2, CH_3, HCO, CH_2O, CH_3O and N_2. Table 1 lists the 25 elementary reactions enumerated as R1 to R25, with reaction rate coefficients. This mechanism contains C1 chemistry, however not C2 or higher C compounds. Similar to [34], but deviating from the original source [35], all reverse reactions were included, and their coefficients determined from the equilibrium constants. It should also be noted that the coefficients of Table 1 are as used by [34], which deviated in R6, R14, R15, while R10 was found in the text (not the table) of [35]. Some trials were made with the original version, denoted “SG(orig)”, where all coefficients are taken from “Table II” of [35]. For rich mixtures, the DRM22 mechanism [36] was used. This is a reduced version of GRI 1.2, consisting of 24 species (including inert Ar and N_2) and 104 reversible reactions. DRM22 showed good laminar flame speed predictions in rich flames at 1 atm [36]. Compared to SG, the six additional species are CH_2, C_2H_2, C_2H_3, C_2H_5, C_2H_6 and Ar.

The full GRI 3.0 mechanism [37] comprised 53 species (including Ar) and 325 reversible reactions of methane oxidation with extensive NO_x chemistry.

The Chemkin and Transport software libraries [38,39] related to chemical mechanism were linked to S3D to provide thermodynamic properties and mixture-averaged transport properties to the solver.

2.3. Hydrogen flux formulation and wall boundary conditions

The membrane hydrogen flux was based Sieverts’ law and expressed as

$$F_{H_2,w} = Q''\cdot W_{H_2}\left(\left(p^{f}_{H_2}\right)^n - \left(p^{p}_{H_2}\right)^n\right), \quad (1)$$

where Q'' is the membrane permanence factor and n is the pressure

exponent. For typical 2–3 μm Pd-based membranes, these were set to $Q'' = 7.0{\cdot}10^{-6}$ kmol/(m^{2}sPa$^{0.5}$) and $n = 0.5$ [40,4]. The wall boundary conditions are well-posed to 1-d domains for IW and PW configurations [41–43]. The temperature and species gradients were set to zero, except for H_2 at the permeable wall, which was determined as

$$\left(\frac{\partial Y_{H_2}}{\partial x}\right)_w = \frac{F_{H_2,w}}{\rho_w D_{mix,w}}. \quad (2)$$

More details of the wall boundary conditions implementation were given in [4,5].

The outlet was treated as non-reflective boundary based on Navier-Stokes Characteristic Boundary conditions (NSCBC) [44,45].

2.4. Definitions of FWI quantities

Flame quenching was defined as the instance where the normalized maximum OH gradient (here denoted OH*) falls or reaches below 0.5. For normalization, the value of the free propagating flame was used. This definition was adopted from laser diagnostics [46,47], where the OH molecule is used to detect the flame front.

The premixed flame position was tracked by three different alternative locations, viz. those of the maximum OH gradient (OH*), the maximum heat release rate ($\dot{\omega}^*_{max}$) and the maximum fuel consumption rate ($-\dot{\omega}^*_{F,max}$). The corresponding flame-wall distances yielded three non-dimensional Peclet numbers.

In a freely propagating flame, the laminar flame speed S_L^0, characteristic flame thickness $\delta_L = \lambda_u/(\rho_u C_{p,u} S_L^0)$, laminar flame power $q_l^0 = \rho_u C_{p,u} S_L^0 (T_b - T_u)$ and thermal flame thickness, $\delta_L^0 = (T_b - T_u)/(\partial T/\partial x)_{max}$, were computed [17,19,1]. The burnt gas temperature T_b was computed as the adiabatic flame temperature for equilibrium at constant pressure. The properties ρ_u, λ_u and $C_{p,u}$ were evaluated at the unburnt gas temperature and initial gas composition.

In the PW cases, the normalizing term for mass flux was F_{H_2max}, which is the maximum wall mass flux evaluated (Eq. 1) for a zero hydrogen partial pressure on the permeate side.

Table 2 lists dimensional quantities and defines the corresponding non-dimensional variables.

2.5. Computational setup and description of cases

The 1-d domain of the head-on quenching setup (Fig. 1) had a total length of $L = 0.02$ m. The grid with uniform mesh had $N = 9984$ nodes, which gave a spatial resolution of $\Delta x = 2.0{\cdot}10^{-6}$ m. These values were chosen in order to capture the flame during quenching. The time step was fixed at $0.5{\cdot}10^{-9}$ s for all simulations. This short time step was due to small chemical time scales for detailed chemistry and acoustics CFL condition. All numerical simulations were distributed on 32 processors.

The freely propagating CH_4-air flame profile generated by Chemkin premix [39] provided the initial field for the S3D code. It was placed in the center of the 1-d domain, i.e. at $x = 0.01$ m, at initial time $t = 0$ s. The initial velocities were set to zero for all cases. The air was assumed as 79% N_2 and 21% O_2, molar based. The pressure of the gas mixture was maintained at 1 atm. All cases were specified with equal wall and unburnt-gas temperature, $T_w = T_u$. The values were 600 K and 750 K. The equivalence ratio was varied as 0.5 (lean), 1.0 (stoichiometric) and 1.5 (rich). These values applied to the initial mixture, unaffected by H_2 influx in the PW cases.

The PW cases had constant feed-side pressure, $p^f_{H_2} = 10.0$ atm, and H_2 permeation occurred from the start of simulation, $t = 0$.

Flame properties for a freely propagating flame were obtained by S3D. Since the Chemkin code is widely used to produce such properties, a comparison was made by using the Chemkin library [38,39] with identical chemical mechanism and specific heats.

The cases with chosen parameters and mechanisms will be specified below, together with the overview of key results in Section 3.1.

The numerical results for the PW configuration were compared against the IW configurations for validation due to lack of experiments, while the results of IW configurations were compared to previous one-dimensional flame quenching of methane premixed flames [10,23].

3. Results

3.1. Overview of cases

Table 3 presents different numerical cases performed. The lean and stoichiometric cases were obtained with the SG mechanism, while the rich cases with DRM22. The spatial resolution was chosen such that the FWI results were independent of mesh size. The number of nodes was maintained at $N = 9984$ for all computations. The number of nodes falling within the flame thermal thickness at quenching, M, was evaluated. It was made sure that this number was at least 40, while 10 points have been regarded as a minimum requirement [3].

3.2. Validation of flame setup and chemical mechanisms

The initialization method for the 1-d transient process was described in Section 2.5, and it yielded marginally deviating flow fields during the flame set-up. Some initial spurious oscillations were observed due to the incorrect velocity field imposed from Chemkin results. Within a short transitional time, the flame re-adjusted within the unburnt mixture and propagated at a nearly constant laminar flame speed (S_L^0) until sensing the presence of the impermeable wall (IW cases) or enriched hydrogen fuel concentration (PW). The short period of incorrect velocity field was ignored for analysis and should have no influence on the final FWI results.

Fig. 2 presents a comparison of basic flame characteristics profiles for Chemkin and S3D after the initialization period. Fig. 2a compares Chemkin profiles of the SG and GRI mechanisms. The profiles from Chemkin are compared to the initialized profiles from S3D in Fig. 2b (SG) and Fig. 2c (GRI). These runs were made for a stoichiometric mixture at 750 K. The S3D results for IW were extracted at 0.55 and 0.39 times the quenching time for SG and GRI, respectively. In the graphs, the abscissa was non-dimensionalized as $(x - x_0)/\delta_L^0$, where x_0 is the location of maximum thermal gradient. Good agreement were observed for the comparisons. Small deviations were observed between the different chemistries, while Chemkin and S3D profiles were virtually identical.

To validate FWI results from the reduced mechanisms (SG, DRM22), some IW cases were computed with GRI 3.0. These were conducted for a temperature of wall and unburnt gas ($T_w = T_u$) at 750 K and equivalence ratios ϕ_u of 0.5, 1.0 and 1.5. This high temperature was chosen to

Table 2
Non-dimensional variables.

Description, quantity	Non-dimensional quantity
Wall heat flux	$\Phi^*_w = \Phi_w/q_l^0$
Flame-wall distance	$y^* = y/\delta_L$
Axial distance	$x^* = x/\delta_L$
Velocity	$u^* = u/S_L^0$
Thermal flame thickness	$\delta_L^* = \delta_L^0/\delta_L$
Time	$t^* = t{\cdot}(S_L^0/\delta_L)$
	$t' = t/t_Q$
Overall heat release rate	$\dot{\omega}^* = \dot{\omega}{\cdot}(\delta_L/q_l^0)$
Fuel (methane) consumption rate	$-\dot{\omega}^*_F = \int_0^L (-\dot{\omega}_F)dx/(\rho_u S_L^0 Y_{F,u})$
Temperature	$T^* = (T - T_u)/(T_b - T_u)$
Wall mass flux	$F^*_{H_2,w} = F_{H_2,w}/F_{H_2max}$
Wall-to-flame distance (Peclet number)	$Pe = y_{(\dot{\omega}_{max})}/\delta_L$
	$Pe_F = y_{(-\dot{\omega}_{F,max})}/\delta_L$
	$Pe_{OH^*} = y_{(OH^*)}/\delta_L$

Table 3
Premixed flame properties obtained for varying ϕ_u with given $N = 9984$ and $p^f_{H_2} = 10$ atm. SG for $\phi_u = 0.5$ and 1.0, DRM22 for $\phi_u = 1.5$.

Wall type	T_w [K]	ϕ_u [–]	S^0_L [m/s]	δ_L [10^{-6} m]	q^0_l [MW/m^2]	T_b [K]	δ^*_L [–]	t^*_Q [–]	$\delta^*_{L,Q}$ [–]	$\Phi_{w,max}$ [MW/m^2]	$\Phi_{w,Q}$ [MW/m^2]	M [–]
IW	600	0.5	0.421	156.38	0.300	1716.80	4.224	63.01	2.186	0.152	0.151	110
IW	600	1.0	1.362	48.23	1.583	2367.50	6.537	208.51	2.342	1.111	0.890	56
IW	600	1.5	0.480	135.47	0.495	2117.30	5.017	74.21	2.339	0.305	0.267	158
PW	600	0.5	0.421	156.38	0.300	1716.80	4.224	38.12	2.284	0.224	≈ 0	178
PW	600	1.0	1.362	48.23	1.583	2367.50	6.537	168.49	6.119	0.139	≈ 0	147
PW	600	1.5	0.480	135.47	0.495	2117.30	5.017	45.92	5.758	0.0167	≈ 0	390
IW	750	0.5	0.938	100.89	0.546	1838.10	4.996	99.54	2.398	0.280	0.259	121
IW	750	1.0	2.146	43.815	2.006	2434.50	6.425	229.15	2.903	1.345	0.989	63
IW	750	1.5	0.921	102.282	0.775	2227.40	4.888	98.12	2.086	0.510	0.490	107
PW	750	0.5	0.938	100.89	0.546	1838.10	4.996	68.69	2.904	0.765	≈ 0	146
PW	750	1.0	2.146	43.815	2.006	2434.50	6.425	190.10	6.045	0.357	≈ 0	132
PW	750	1.5	0.921	102.282	0.775	2227.40	4.888	63.34	5.393	0.092	≈ 0	276

give a higher flame speed and flow velocity, shorter transit time and, accordingly, lower computational cost. Furthermore, one case of stoichiometric mixture at the low temperature of 300 K was carried out for comparison to results of Ganter et al. [34]. The wall heat flux and the time were non-dimensionalized as described in Section 2.4. It can be noted that the quenching times differed between this and previous investigations [34,10,23], since the initial flame locations and lengths of computational domains were not the same. These parameters should not influence on the obtained FWI results.

Table 4 presents the characteristics for the compared cases. The SG chemistry gave somewhat higher flame speeds than GRI during FWI, with corresponding differences for other quantities. Also shown is comparison of SG as used here (from [34]) and "SG(orig)" with the original coefficients of [35] (see Section 2.2). The seemingly small modifications gave notable improvement.

Fig. 3 presents the normalized wall heat fluxes for SG and GRI for wall temperatures of 300 K ($\phi_u = 1.0$) and 750 K ($\phi_u = 0.5$, 1.0 and 1.5). The mechanisms showed good agreement in terms of heat flux profiles, except for the rich mixture. At 750 K, SG gave a moderate under-prediction in comparison to GRI of the wall heat flux for lean and stoichiometric conditions. These deviations occurred primarily during quenching. For the rich mixture, SG failed. The peak of the wall heat flux was 38% lower compared to GRI. On the contrary, DRM22 gave very good agreement with GRI for the rich mixture, indicating that C2 compounds play a notable role.

In the following, computations are performed at wall temperatures of 600 K and 750 K for IW and PW configurations with SG for $\phi_u = 0.5$ and 1.0, and with DRM22 for $\phi_u = 1.5$.

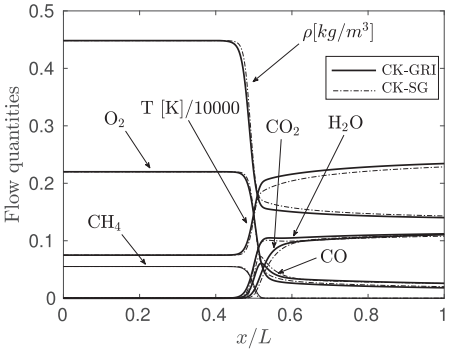

(a) GRI 3.0 vs. SG in Chemkin (CK)

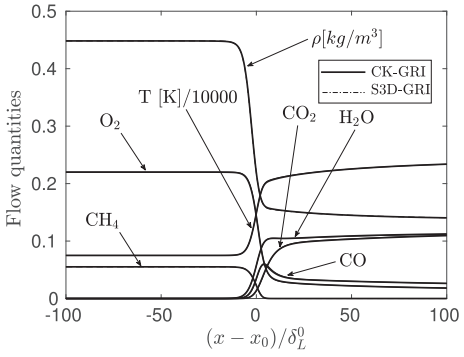

(b) Chemkin (CK) vs. S3D, both with GRI 3.0

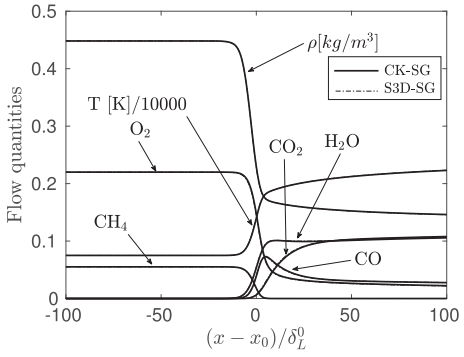

(c) Chemkin (CK) vs. S3D, both with SG

Fig. 2. Temperature, major species mass fractions and density profiles from Chemkin and S3D codes for SG and GRI 3.0 mechanisms. Free propagating laminar premixed methane flame. The unburnt mixture was stoichiometric at 750 K.

Table 4
Premixed flame properties for different ϕ_u conditions for IW configurations at T_w = 300 K and 750 K.

ϕ_u [–]	N [–]	T_w [K]	Mech [–]	S_L^0 [m/s]	$\dot{\omega}_{max}$ [10^9 W/m^3]	δ_L [10^{-6} m]	δ_L^* [–]	$\delta_{L,Q}^*$ [–]	$\dot{\omega}_{Q\,max}/\dot{\omega}_{max}$ [–]	q_l^0 [MW/m^3]	$\Phi_{w,max}^*$ [–]	$\Phi_{w,Q}^*$ [–]
1.0	9984	300	SG(orig)	0.538	6.979	37.420	9.736	2.824	3.919	1.245	0.667	0.662
1.0	9984	300	SG	0.384	4.667	52.111	8.250	1.913	0.974	0.894	0.638	0.634
1.0	9984	300	GRI	0.381	4.393	53.376	8.005	1.901	0.701	0.887	0.643	0.639
0.5	9984	750	SG(orig)	1.072	1.935	88.252	5.352	2.207	0.603	0.624	0.548	0.508
0.5	9984	750	SG	0.938	1.689	100.89	4.996	2.398	0.212	0.546	0.512	0.474
0.5	9984	750	GRI	0.830	1.825	113.91	4.259	2.125	0.213	0.483	0.569	0.544
1.0	9984	750	SG(orig)	2.763	16.047	34.015	7.602	2.400	2.820	2.585	0.712	0.526
1.0	9984	750	SG	2.146	12.133	43.815	6.425	2.903	0.710	2.006	0.670	0.493
1.0	9984	750	GRI	2.007	11.043	46.832	6.027	2.976	0.558	1.877	0.702	0.684
1.5	9984	750	SG(orig)	2.198	11.642	42.881	6.166	2.091	1.621	1.850	0.878	0.856
1.5	9984	750	SG	0.646	1.630	145.873	4.529	1.981	0.315	0.543	0.407	0.329
1.5	9984	750	DRM22	0.921	2.760	102.282	4.888	2.086	0.453	0.775	0.658	0.632
1.5	9984	750	GRI	0.945	2.926	99.678	4.861	2.222	0.508	0.796	0.656	0.636

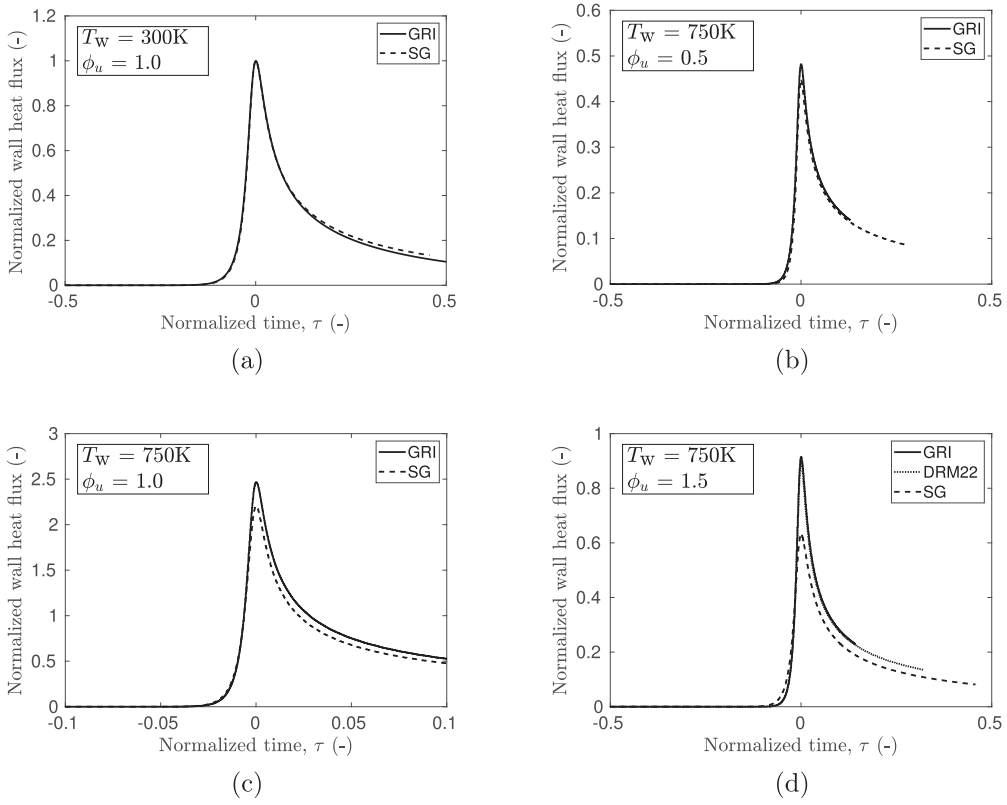

Fig. 3. Development of normalized wall heat fluxes for IW: SG and DRM22 compared to GRI 3.0. The quenching wall heat flux at T_w = 300 K, ϕ_u = 1.0 with GRI was used for normalization. The abscissa is $\tau = (t - t_Q)/t_Q$, where t_Q is the quenching time.

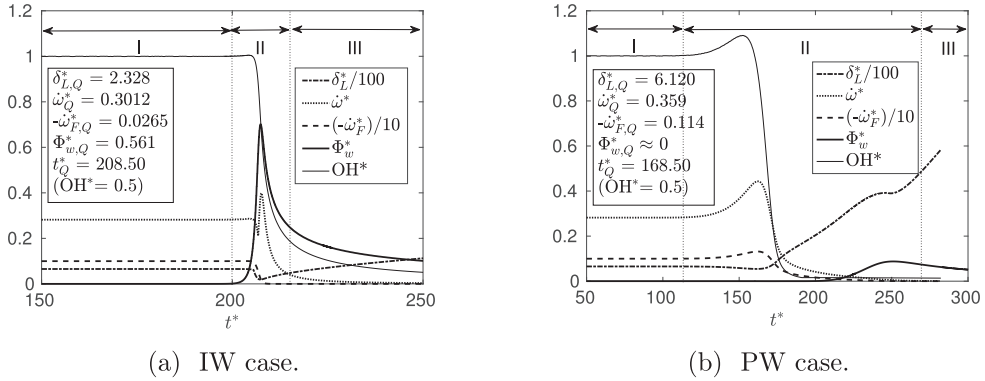

Fig. 4. Non-dimensional FWI characteristic parameters at T_w = 600 K and ϕ_u = 1.0. The values at quenching are included.

3.3. Flame-wall interaction characteristics

The head-on flame quenching process can be described by FWI global parameters. The global development could be subdivided into three stages [17,5] as seen in Figs. 4 and 5: Undisturbed propagation, Stage I, influence of wall to propagating flame, Stage II, including quenching, and Stage III after quenching with overall decrease of fuel reaction and heat release rates. For IW, the propagating flame sensed the wall influence at $t^* = 200$, while much earlier for PW, at $t^* = 115$.

Figs. 4 and 5 present non-dimensional temporal profiles of FWI characteristics (δ_L^*, $-\dot{\omega}_F^*$, $\dot{\omega}^*$, Φ_w^*, OH*, Pe, Pe_F, Pe_{OH^*}) of IW and PW configurations for stoichiometric conditions, $T_u = T_w = 600\,K$, $p_{H_2}^f = 10\,atm$ and $N = 9984$.

In Stage I, the flame propagates as an undisturbed laminar flame. The flame thickness, primary-fuel (methane) consumption rate and heat release rate reached steady values at $\delta_L^* = 6.54$, $-\dot{\omega}_F^* = 9.99$ and $\dot{\omega}^* = 0.282$. For IW Stage II, the fuel consumption rate declined towards zero during quenching and then remained zero. The heat release rate declined before quenching to $\dot{\omega}^* = 0.211$ at $t^* = 206.8$, then rapidly reached a peak value of 0.399 at $t^* = 207.6$, and declined after quenching. The peak wall heat flux was $\Phi_w^* = 0.702$ at $t^* = 207.4$, where the thermal flame thickness reached a minimum value, $\delta_L^* = 1.90$. Thereafter, the flame broadened. Quenching occurred at $t^* = 208.5$, as defined by the OH gradient (cf. Section 2.4). Accordingly, the quenching instance was close to the peak wall heat flux. The wall-to-flame distance based on reaction heat release, Pe, reached zero at $t^* = 206.8$, while Pe_F and Pe_{OH^*} reached minimum values of 1.91 and 2.49, respectively, at quenching.

For PW, the wall hydrogen permeation shortened Stage I, while Stage II was about 10 times longer than for IW. The primary-fuel consumption and the heat release rates peaked in Stage II with $-\dot{\omega}_F^* = 0.132$ and $\dot{\omega}^* = 0.443$, both at $t^* = 162.7$. From its peak, $\dot{\omega}^*$ declined to 0.359 at $t^* = 168.5$ (quenching) and further to a low value. The primary-fuel consumption rate $-\dot{\omega}_F^*$ declined gradually after its peak value, while the flame thickness grew from $t^* = 162.7$ and was $\delta_L^* = 6.12$ at quenching. The wall-flame distance according to the different definitions, Pe, Pe_{OH^*} and Pe_F, was virtually the same and reached 49.4 at quenching (Fig. 5b). That is, contrary to IW, quenching occurred away from the wall for PW.

3.4. Development through quenching

Fig. 6 displays the temporal development of profiles of reduced temperature, velocity and total reaction heat release for IW and PW. The profiles remained virtually unchanged until $t' = t/t_Q = 0.95$ or $t^* = 198.1$ for IW, and until $t' = 0.90$ or $t^* = 151.6$ for PW. Similarly, Figs. 7–10 show profiles of selected species.

The peak temperature gradient of IW reached to 3.45 times the maximum temperature gradient of the free propagating flame. In comparison, Popp and Baum [10] found a value of 4.0 at quenching. The difference can be attributed to differences in chemical mechanism, numerical method and grid. After quenching, a remaining, much weaker reaction zone expanded for both IW and PW. For IW, the gas velocity decreased gradually and became negative, while PW showed higher (positive) values indicating the hydrogen flow across the wall.

Besides the obvious occurrence of permeated H_2 near the wall for PW, the notable difference from IW was the unreacted major species. Fig. 7 shows considerable amounts of CH_4 and O_2 remaining near the wall after quenching for PW. For IW, these species were nearly consumed, while modest amounts of H_2 and CO (Fig. 9e) were left. Among minor species, it was noted some accumulation of HO_2 in front of the flame for both configurations (Fig. 9c–d), more for PW than for IW. Similarly, and to greater extent, H_2O_2 was accumulated in front of the flame, increased in the flame and, for PW, remained left over after quenching, Fig. 8d.

Behind the propagating flame, the O_2 level was significantly lower for PW than for IW (Figs. 7c–d). On the contrary, the corresponding CO level was higher. It was also noted that the burnt-mixture temperature for PW decreased towards quenching.

Radicals H, O, OH were formed in the flame and partly consumed (Fig. 9) in both configurations. For PW, O and OH declined before quenching. This decline started before the flame reached the maximum heat release rate ($t' = 0.966$) for PW, while for IW their peaks were maintained to this point (at $t' = 0.996$).

For IW, it was seen that the flame front continued almost unchanged from the free propagation state close up to the wall before quenching. This was also consistent with the development of the heat release rate and fuel reaction rate seen in Fig. 4a. The initial reactants CH_4 and O_2 were to a large extent consumed during the process, and the final mixture approached that of the adiabatic equilibrium product.

The IW flame propagated against a flow caused by heating and expansion (Figs. 6c, e). In addition to said effects, the PW flame faced a flow enchanced by permeating gas. This, combined with an increasing heat release (Fig. 6f) and expansion, gave a larger velocity against the flame propagation. Although the heat release increased, the temperature gradient of the flame front showed a moderate increase from $t' = 0.98$. Furthermore, the overall temperature rise, i.e. the burned temperature, had a minor decrease.

The notable difference from IW, was the early, off-wall quenching of the PW flame. High concentrations of the main reacants CH_4, H_2 and O_2 were left behind in the near-wall zone after quenching (Figs. 7b, d, f). As the flame propagated against the increasingly richer near-wall zone, the reaction heat release increased (Fig. 6f). Similarly, several intermediates from the methane and hydrogen consumption increased. CO had a minor increase in the flame zone, while an increasing amount was left behind the flame (Fig. 9f). On the other hand, the accumulation of

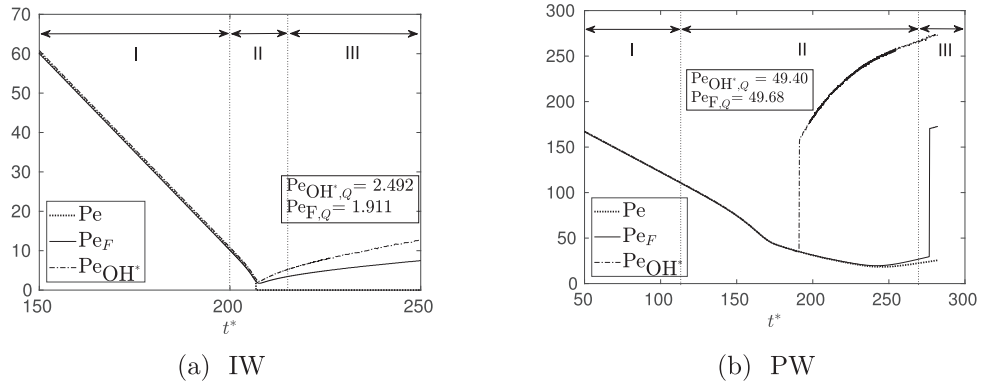

(a) IW (b) PW

Fig. 5. Peclet numbers versus non-dimensional time for $\phi_u = 1.0$ and $T_w = 600\,K$. The values at quenching are included.

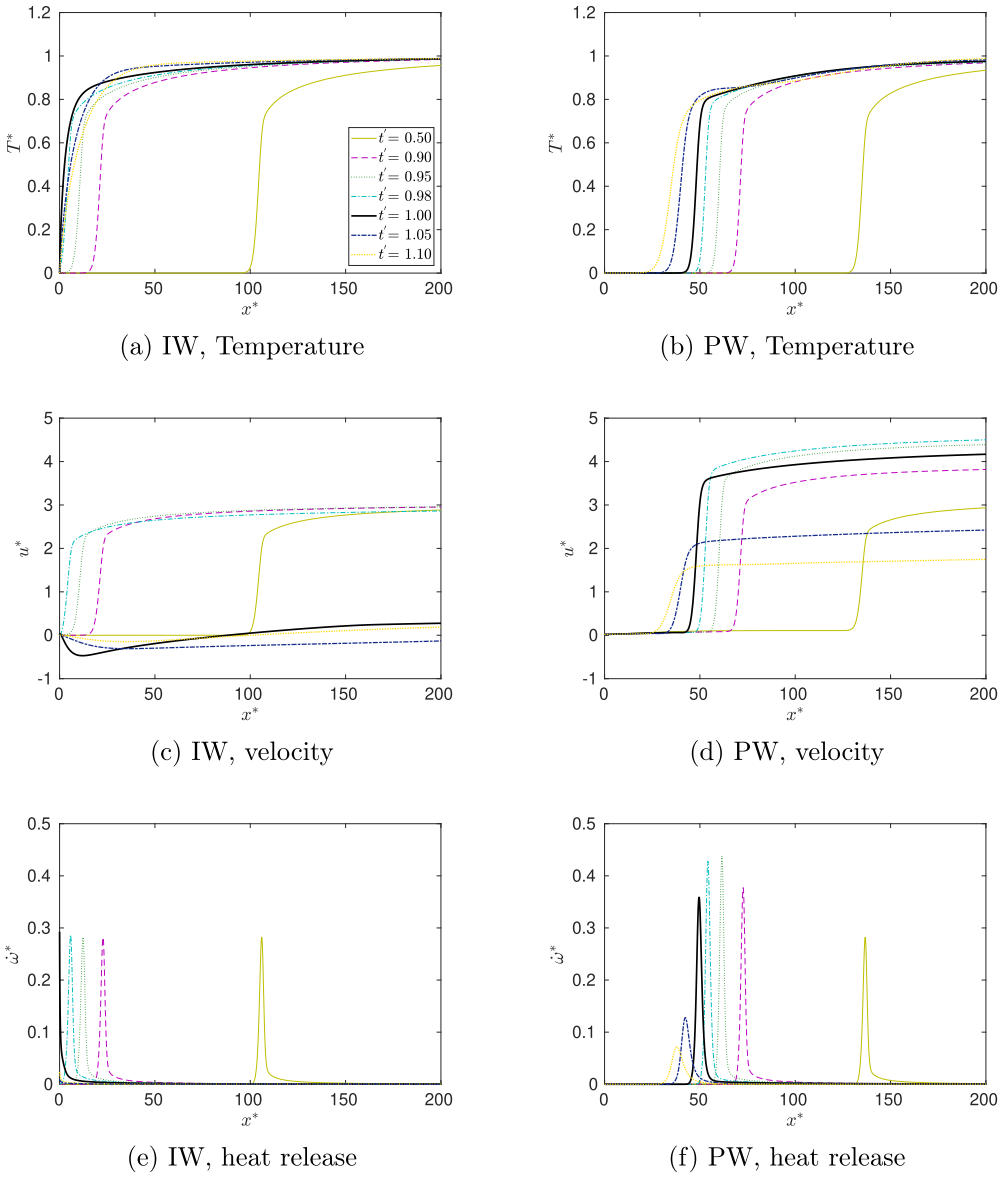

Fig. 6. Non-dimensional temperature, gas-flow velocity and total reaction heat release rate at different times of FWI for $\phi_u = 1.0$ and $T_w = 600$ K. $t' = 1$ represents flame quenching time.

O and O_2 decreased (Figs. 10d,f).

The species balance can be expressed as

$$T_k = \frac{\partial}{\partial t}(\rho Y_k) = C_k + D_k + R_k, \tag{3}$$

where the three right-hand-side terms denote, respectively, the contributions of convection, diffusion and reactions to the transient accumulation of the species (left-hand side). An analysis of the species balances (Convection-Diffusion-Reaction, CDR) showed that the changes of OH and O_2 became visible earlier than for other species. Fig. 11 shows the CDR budgets of OH at different times through quenching for PW. Deviations from the free propagation became visible from $t' = 0.90$. Smilar developments were seen for the other species, however visible later, from $t' = 0.95$ (most species) or $t' = 0.98$ (H_2O_2, H, H_2O). The corresponding graphs for the IW case showed only minor changes until after $t' = 0.98$. These were similar (apart from the effects of the deviating unburned temperature) to those of Jiang et al. [9]. It can be noted that the quenching definition applied by said authors corresponded to $t' = 0.976$ of the present work.

3.5. Heat release rate and individual reactions

Fig. 12 presents temporal non-dimensional heat release rates. The total heat release rate is also shown in Fig. 4, toghether with the wall heat flux and the fuel (methane) reaction rate. At peak wall heat flux, the heat release rate reached 1.37 times that of the undisturbed laminar flame for IW. At quenching, this value was 1.02. For PW, quenching occurred when the heat release was 1.30 times that of free propagation, whereas only 0.016 at the peak wall heat flux. The breakdown of elementary reactions during freely propagating and quenching states for IW and PW are displayed in Table 5. Here, the heat release rate of individual net two-way reactions are evaluated at the location of the maximum total heat release rate.

In front of the propagating flame, H_2 was present (also for IW), together with HO_2 H_2O_2 and CH_3. The HO_2 was produced from R5(f), and then converted to H_2O_2 through R21(f), which had a peak ahead of the flame front. Both these reactions had zero activation energy, and occurred at low temperature. The latter reaction had minimal contribution in the flame zone. When approaching the flame, H_2O_2 was

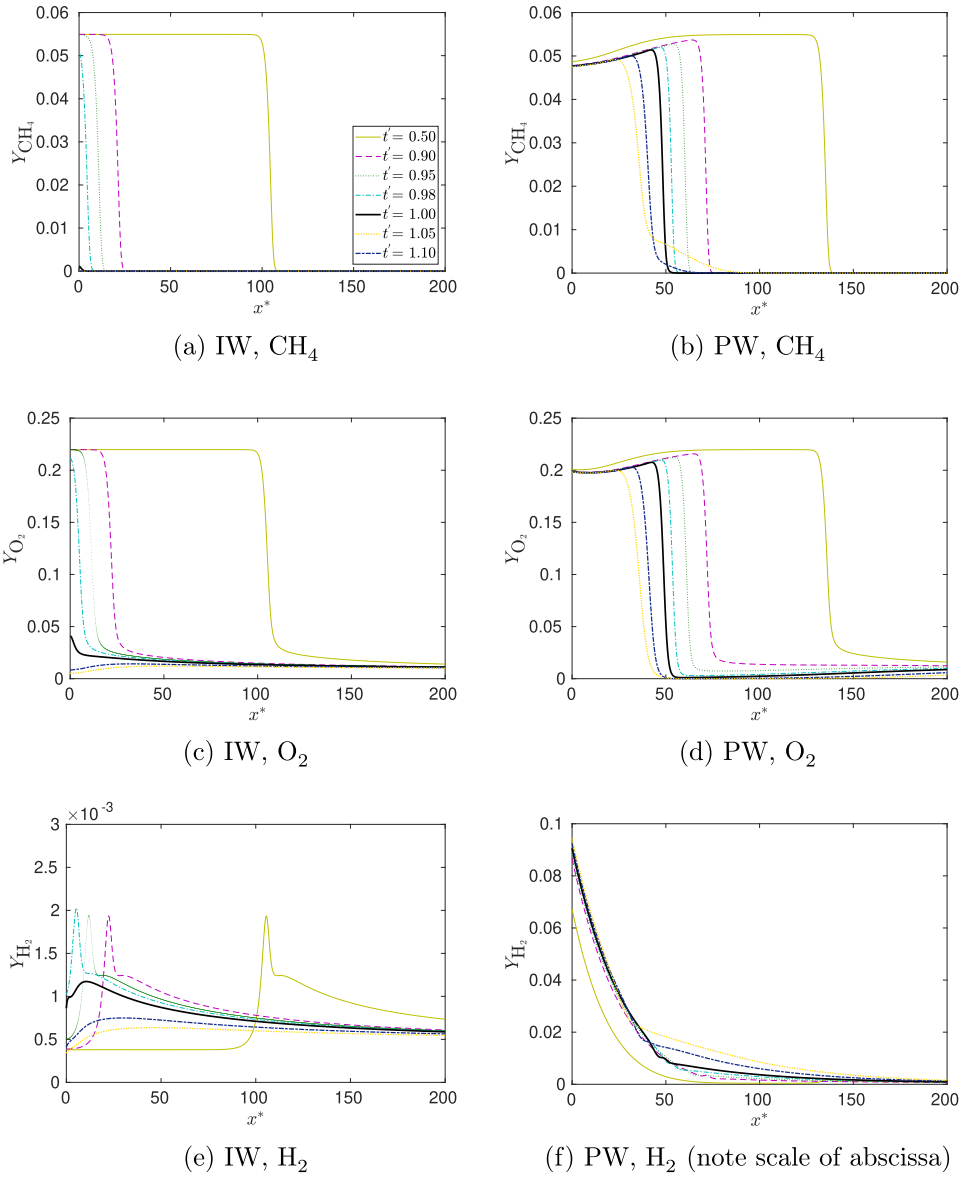

(a) IW, CH_4 (b) PW, CH_4

(c) IW, O_2 (d) PW, O_2

(e) IW, H_2 (f) PW, H_2 (note scale of abscissa)

Fig. 7. Species mass fraction profiles of CH_4, O_2 and H_2 at stoichiometric conditions, 600 K, for IW and PW. $t' = 1$ represents flame quenching time.

consumed by R22(f) and, to lesser extent, by R23(f). Other radical and intermediate species had a net production primarily in the flame zone, while declining after the flame front.

In the case of IW, R5(f) increased strongly towards quenching at the wall. Also R23(f) and R21(f) increased, consuming H_2O_2 now produced in the reversed R22. From Table 5 it is seen that the 9 most important reaction in the free flame (7 exothermic, 2 endothermic) almost completely lost their contributions at quenching, while others rose to maintain a comparable total heat release.

For PW, the importance of the reactions were maintained into quenching. Subsequently, the decaying reactions still generated some heat, and the wall heat flux reached a peak at $t^* = 250.1$. At this instance, the exothermic R10(r), R3(f), R5(f) and endothermic R1(f) caused about 90% of the total heat release.

3.6. Effects of varying equivalence ratio and temperature

Fig. 13 presents transient wall heat and mass fluxes at ϕ_u of 0.5, 1.0 and 1.5 for $T_w = 600$ K. For PW, the feed pressure $p^f_{H_2}$ was maintained at 10 atm. The varying equivalence ratios led to different free flame characteristics such as flame thickness and laminar flame speed and had significant influence on wall fluxes during flame quenching.

Table 3 showed that the highest combustion temperature and flame speed are obtained for $\phi_u = 1.0$. These values were lowered with increasing departure from stoichiometric conditions. For IW, the (dimensional) peak and quenching wall heat fluxes also had this tendency. For PW, however, it was an order of magnitude lower compared to IW for $\phi_u = 1.5$ and 1.0, while higher for $\phi_u = 0.5$. For IW with $\phi_u = 1.0$, radicals accumulated in the near-wall region owing to thermal loss from flame to wall. The radicals H, O and OH led to exothermic low-activation reactions with single peaks of heat release rate at the wall during FWI. These peaks resulted in a large wall heat flux at flame quenching. Fig. 13a shows that for IW, $\phi_u = 1.0$ led to the highest non-dimensional peak wall heat flux at the earliest quenching time (dimensional), while $\phi_u = 1.5$ and $\phi_u = 0.5$ had slightly lower peaks. The peak magnitudes of wall heat fluxes were primarily depending on the near-wall reaction heat release. At quenching for stoichiometric conditions, the main reactions R5(f), R24(f), R6(f) and R7(f) in decreasing order contributed 81.47% of the total heat release at the wall. Moreover, HO_2 and H_2O_2

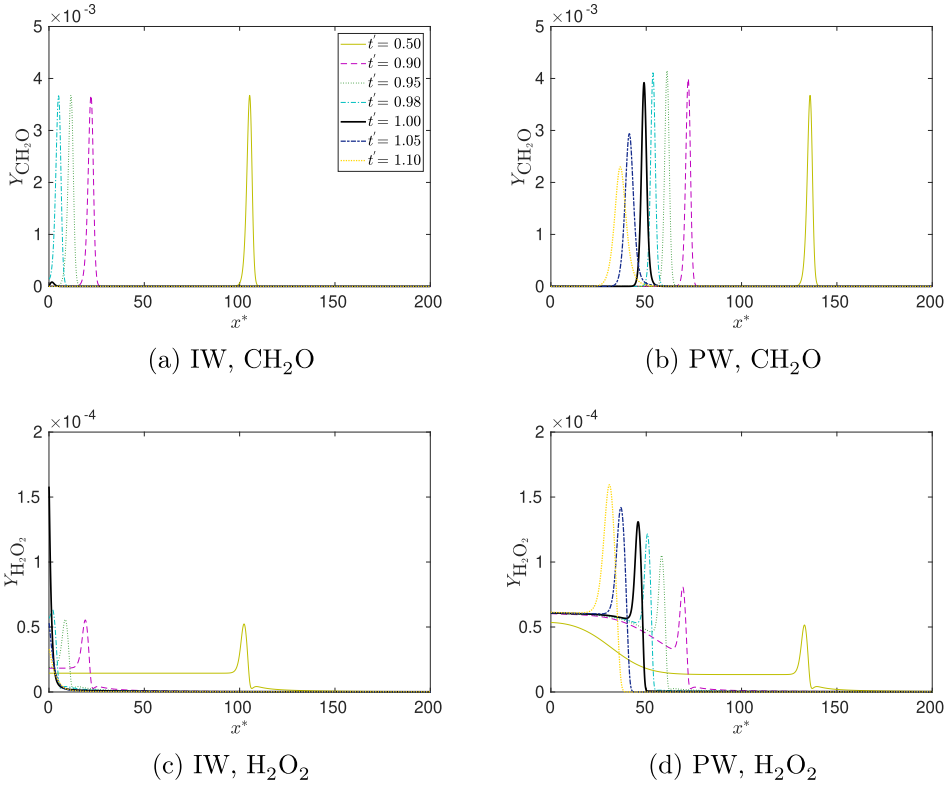

Fig. 8. Species mass fraction profiles of CH_2O and H_2O_2 at stoichiometric conditions, 600 K, for IW and PW.

had accumulated at the quenching instance.

In the rich flame, excess fuel led to main exothermic reactions in decreasing order (DRM22 reactions numbered consecutively from [36]), R34(f) [$H + CH_3 + M \rightarrow CH_4 + M$], R6(f) [$O + CH_3 \rightarrow H + CH_2O$], R92(f) [$2CH_3 + M \rightarrow C_2H_6 + M$] and R49(f) [$OH + H_2 \rightarrow H + H_2O$] and endothermic reaction R24(f) [$H + O_2 \rightarrow O + OH$] contributing 75.41% of the total heat release at wall. The C2 chemistry played a significant role, contributing 21.12% of the total heat release rate at flame quenching, including 16.63% from R92(f). The lowest peak of heat release occurred in the lean mixture, with excess of radicals OH and O in the near-wall region. It was seen that at quenching R13(f) [$O + C_2H_2 \rightarrow CO + CH_2$], R5(f) [$O + CH_2(s) \rightarrow H + HCO$] and R15(f) [$O + C_2H_5 \rightarrow CH_3 + CH_2O$] in decreasing order contributed 80.26% of the total heat release at the wall.

For the PW configuration, the wall heat flux variation (primarily) depended on the initial mixture composition and the accumulated H_2 wall flux, which promoted a pool of H during the FWI process. This resulted in enhanced heat release at some distance from the wall.

As with IW, PW had the earliest quenching at $\phi_u = 1.0$. For all three stoichiometries, the main reactions were, in decreasing order, R13(f), R10(r), R3(f), R5(f), while R1(f) had a notable endothermic contribution to the large heat release rate (for DRM22, the same reactions, although with other numbers). The combined contributions of said reactions were 90.45%, 85.61% and 45.92% of the total heat release for $\phi_u = 0.5$, 1.0 and 1.5, respectively.

Compared to IW, quenching was delayed for stoichiometric and rich mixtures, with peak wall heat fluxes reduced to 0.125 and 0.055, respectively, for $\phi_u = 1.0$ and 1.5, of the IW values. On the other hand, the lean case ($\phi_u = 0.5$) led to earlier quenching with a peak wall heat flux 1.467 times that of IW.

The transient wall H_2 mass fluxes of PW are shown in Fig. 13b. All conditions showed a decreasing trend of the non-dimensional $F^*_{H_2,w}$ until quenching. The flux reflected the changing content of H_2, Eq. (1), and for the rich case, the flux increased after quenching.

The wall and unburnt-gas temperature was increased from 600 to 750 K, while the feed pressure $p^f_{H_2}$ of 10 atm was maintained. Fig. 14 presents normalized wall fluxes for the IW and PW configurations for varying equivalence ratios. The normalized wall fluxes showed trends for IW and PW similar to those observed for 600 K. However, the increase in wall heat flux from 600 to 750 K was notably larger for PW than for IW. Yet, the dimensional peak values (Table 3) were less for PW than for IW at $\phi_u = 1.5$ and 1.0. For the lean mixture, PW had notably higher heat flux compared to IW.

The quenching Peclet number $Pe_{OH^*,Q}$, i.e. flame-wall distance, is presented in Fig. 15 for IW and PW for the two wall temperatures and three equivalence ratios. It should be noticed here that the lines between data points are included for readability, not necessarily showing the variation between the points. For IW, the dimensional distance was clearly shorter for the stoichiometric case (lesser δ_L) than for lean and rich. For PW, the distance increased with the equivalence ratio. At the higher wall temperature, the flame came closer to the wall, except for the rich PW case.

4. Discussion

4.1. Influence of thermal radiation

In the present study, radiation heat transfer was neglected, which is in agreement with previous research in methane [14,16,48,10] and hydrogen flames [17,19,18,5]. A simplified evaluation of heat transfer from the hot gases to the wall can be performed through post processing calculations using the optically thin flame assumption [49,50]. Previous estimates [5] performed for hydrogen flames showed that the radiation heat transfer was 6 orders of magnitude less than the total reaction heat release rate during free propagation and quenching of the flame.

A similar estimate was made for the present stoichiometric methane flame at the highest unburnt temperature (750 K). It showed that the total reaction heat release was 4 orders of magnitude larger than the

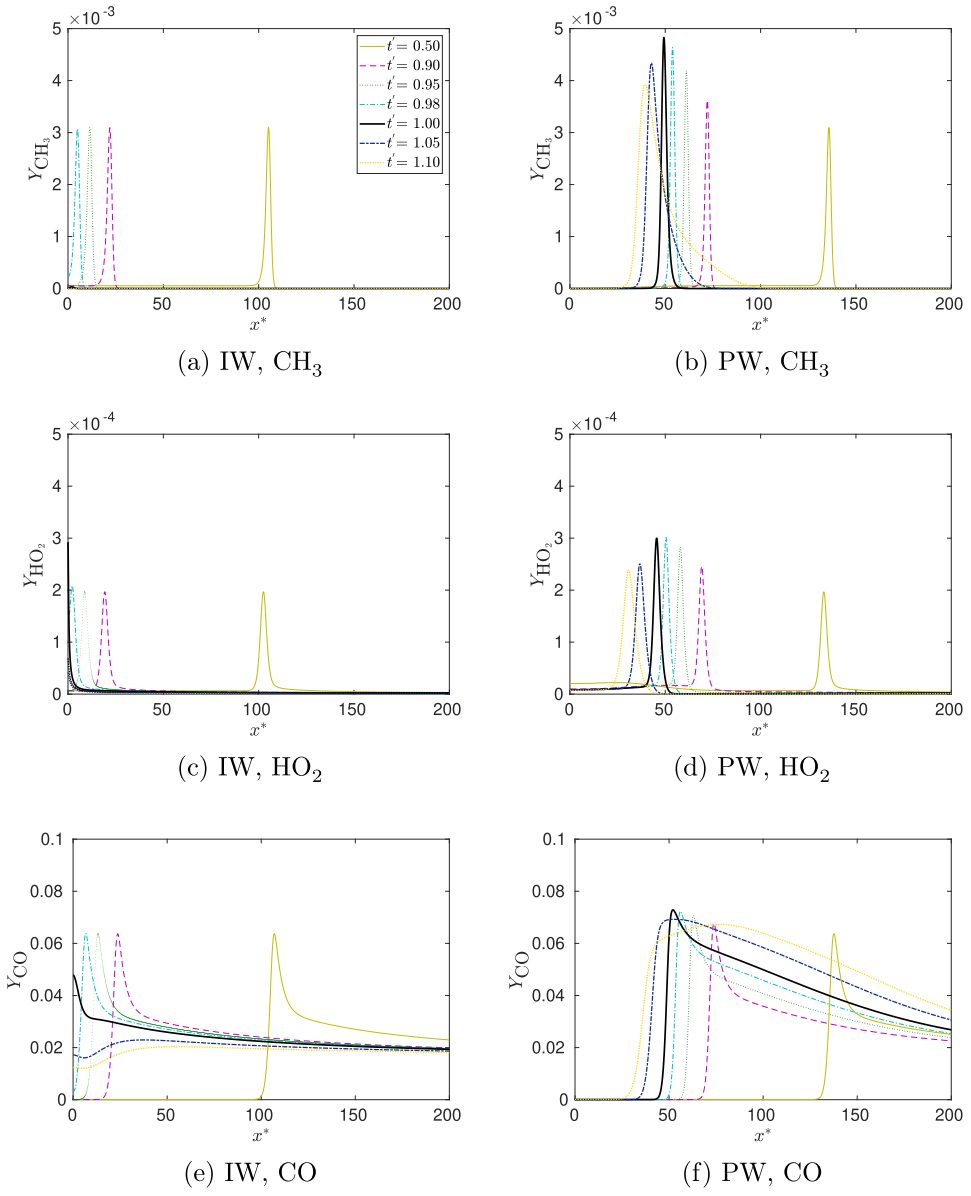

Fig. 9. Species mass fraction profiles of CH_3, HO_2 and CO at stoichiometric conditions, 600 K, for IW and PW.

emitted radiation heat. Near quenching at the wall, the ratio increased to 5 orders of magnitude. Consequently, neglecting radiation heat transfer appeared to be justified for this configuration.

4.2. Validity of chemical mechanisms

The reduced mechanisms SG and DRM22 were regarded to meet the requirements for lower computational costs, while use of a full mechanism like GRI 3.0 was considered as too demanding. For comparison with SG and DRM22, some IW cases were simulated with GRI 3.0 (Section 3.2 with Table 4). The SG mechanism provided sufficiently good results for lean and stoichiometric conditions. However, it failed for the rich mixture, as could be expected in the absence of C2 chemistry and higher carbon-chain reactions. DRM22 showed good agreement with GRI for rich flames. It was seen (Section 3.6) that the C2 reactions of DRM22 had notable contributions to the total reaction heat release. Therefore, DRM22 was employed for $\phi_u = 1.5$, while the simpler (cheaper) SG for $\phi_u = 0.5$ and 1.0.

4.3. Definitions of flame quenching

Various definitions of the quenching instance and flame position can be found in literature. Westbrook et al. [6] choose the iso-contour at 1500 K (for $T_u = 300$ K) nearest to the wall as he flame position, and defined quenching at the instance where this distance had its minimum value.

Others have used the instance of the maximum wall heat flux as the criterion for quenching. With this definition, the flame position has been chosen as a more or less arbitrary temperature iso-line, such as 1900 K [23] or $T^* = 0.9$ [48], the position of the maximum heat release rate ($\dot{\omega}^*$) [22,10,17] or the position of maximum fuel consumption rate ($-\dot{\omega}_F^*$) [17]. Each of these positions constituted the quenching distance when the quenching occurred.

In the spirit of Westbrook et al. [6], the instance of the minimum thermal flame thickness δ_L^0 could be taken as the quenching instance.

Another potential criterion is the instance of peak maximum reaction heat release. Then, its location at this instance can determine the quenching distance. A further possibility (e.g., [9]) is to define the flame position by the location of maximum fuel (methane)

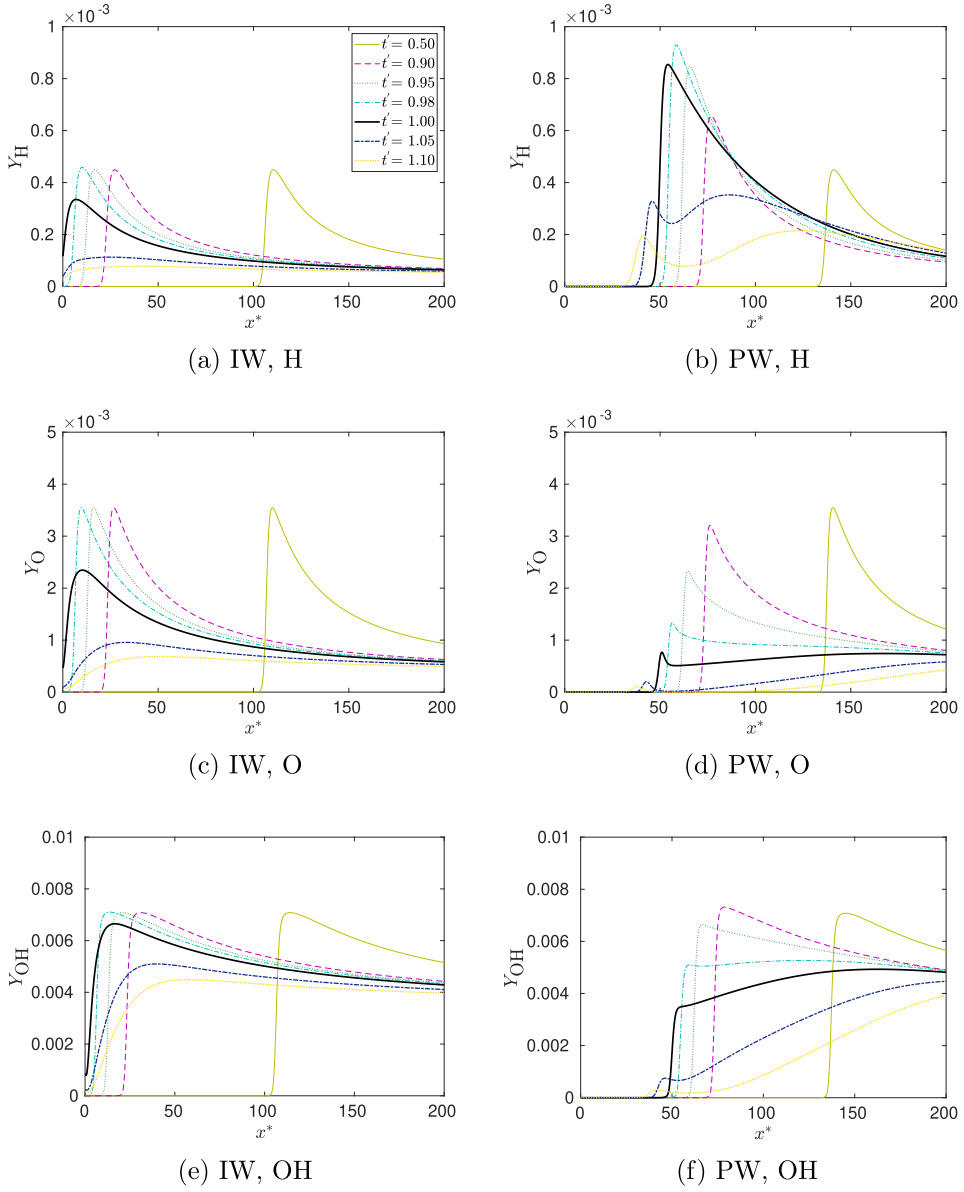

Fig. 10. Species mass fraction profiles of radicals H, O and OH at stoichiometric conditions, 600 K, for IW and PW.

consumption. The quenching instance is the time of the minimum wall-flame distance, and the quenching distance is this distance.

A different approach was chosen by [46], defining quenching to the instance when the spatial OH gradient fell below half its maximum value. The point of maximum instantaneous OH gradient was taken as the flame position and hence, the quenching distance. This definition was explained and used above, Section 2.4.

Table 6 compares the quenching instance according to the different criteria together with the associated flame-wall distances for the case of $\phi_u = 1.0$ and $T_w = 600$ K. The results illustrated that, for this specific IW case, the choice of quenching-instance criterion would give a minute impact on the result. For the PW case, however, the maximum wall-heat flux criterion appeared unsuitable. This could also be seen from the transient profiles of Fig. 4b.

A related issue is the time-scale for flame-wall interaction. This has been defined [22,13] as the time required for Φ_w to increase to its maximum from half of this value. For the present PW cases, this timescale loose its significance.

4.4. Head-on quenching process

Above, e.g. in Figs. 4–5, the global development was subdivided into three stages following Dabireau et al. [17]. This description was clearly suitable for the IW cases. The study of H_2/air [5] showed this development, as well, both for IW and PW. The present PW case showed similarities to these, but also deviations. An alternative description could be in four stages, where the present Stage II is split into two: one comprising quenching and one including the later increasing and peaking wall heat flux.

The reasons for the early, away from wall, quenching in the PW cases can be a combination of factors. First, it can be noted that the amount of permeated H_2 was considerable. Up to quenching for the case of $T_w = T_u = 600$ K and $\phi_u = 1.0$, the amount of substance of permeated H_2 exceeded the amount of CH_4 initially present in the domain. The molar fraction of H_2 became high near the wall, above 50%. In spite of this, there was still a significant amount of O_2 left at quenching. Hence, lack of oxidizer was not the primary reason for quenching. The high near-wall H_2 concentration can be relevant for the near-wall zone

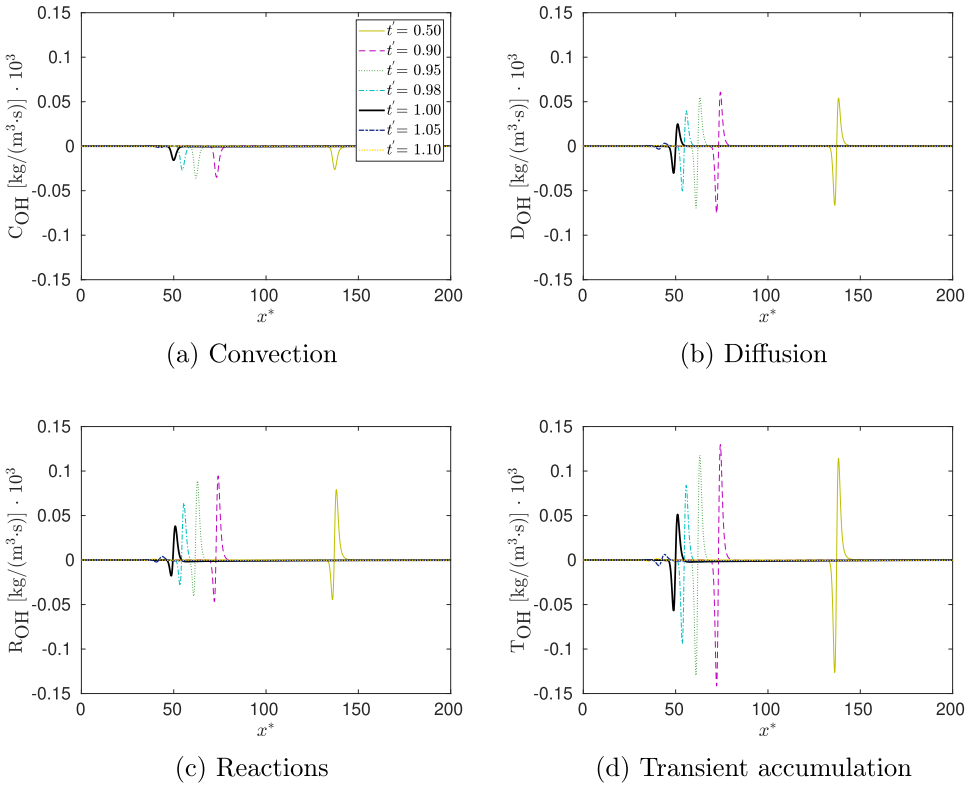

Fig. 11. Convection–Diffusion-Reaction balances of OH at different times near quenching for PW of ϕ_u = 1.0 and T_w = 600 K. C, D and R show contributions to OH accumulation (T) due to, respectively, convection, diffusion and reactions.

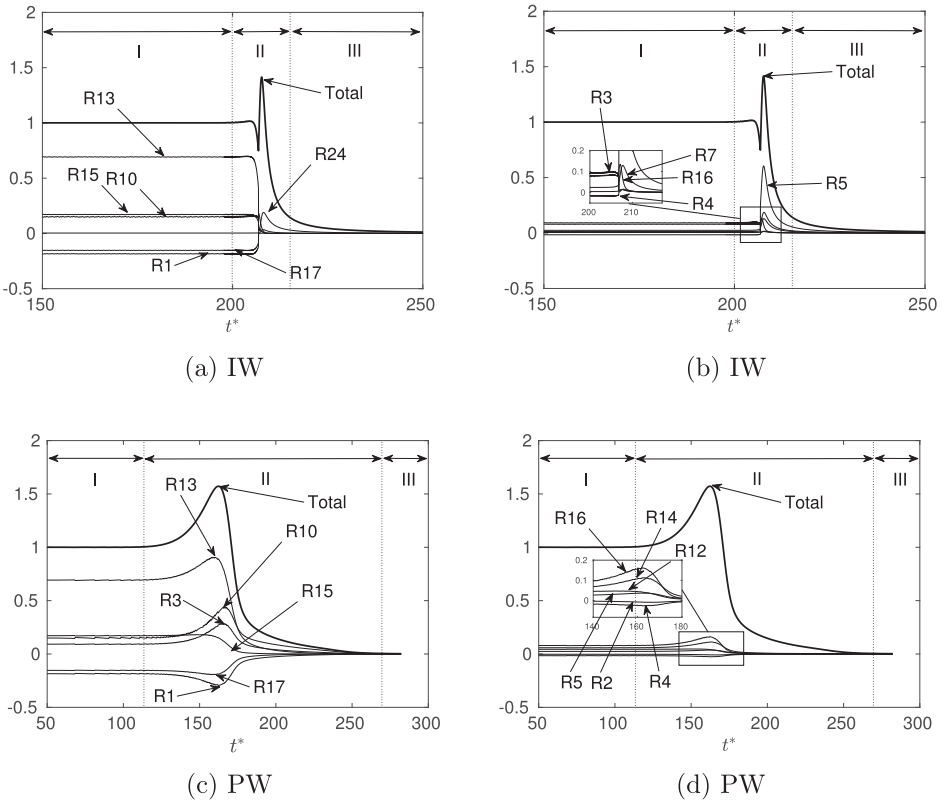

Fig. 12. Non-dimensional heat release profiles for total (overall) heat release rate and individual reactions at ϕ_u = 1.0 and T_w = 600 K. The total heat release rate of the freely propagation flame was used for normalization.

Table 5
Heat release rate of individual reactions (% of the total heat release rate) at $\phi_u = 1.0$ and $T_w = 600$ K for the freely propagating flame, and for quenching at IW and PW. Net reactions are forward (f) or reverse (r).

Free prop.		IW at t_Q^*		PW at t_Q^*	
Reaction	%	Reaction	%	Reaction	%
R13(f)	69.113	R5(f)	41.276	R13(f)	48.922
R15(f)	17.143	R24(f)	16.969	R10(r)	32.222
R10(r)	14.783	R6(f)	13.732	R3(f)	20.579
R3(f)	9.243	R7(f)	9.500	R16(f)	8.495
R16(f)	7.955	R8(f)	3.246	R14(f)	7.109
R14(f)	5.850	R9(f)	2.968	R15(f)	6.637
R12(f)	4.381	R1(r)	2.871	R5(f)	2.363
R9(f)	2.481	R16(f)	1.890	R12(f)	2.130
R5(f)	2.421	R25(f)	1.695	R6(f)	1.375
R6(f)	1.335	R22(r)	1.691	R9(f)	0.847
R7(f)	0.462	R4(f)	1.266	R7(f)	0.472
R24(f)	0.339	R3(f)	0.905	R24(f)	0.239
R8(f)	0.259	R10(r)	0.842	R19(f)	0.161
R19(f)	0.108	R15(f)	0.302	R25(f)	0.152
R25(f)	0.070	R13(f)	0.299	R8(f)	0.087
R23(f)	0.003	R23(f)	0.203	R23(f)	0.001
R21(f)	0.000	R17(r)	0.191	R21(f)	0.000
R20(f)	−0.001	R12(f)	0.083	R20(f)	−0.001
R22(f)	−0.016	R21(f)	0.071	R22(f)	−0.051
R18(f)	−0.039	R14(f)	0.000	R18(f)	−0.062
R11(f)	−0.177	R18(r)	0.000	R11(f)	−0.190
R2(f)	−0.271	R19(f)	0.000	R2(f)	−0.663
R4(r)	−1.609	R20(r)	0.000	R4(r)	−1.792
R17(f)	−15.343	R2(f)	0.000	R17(f)	−10.562
R1(f)	−18.492	R11(f)	0.000	R1(f)	−18.471

of a membrane combustor, although not for the overall combustor volume.

Second, the burnt temperature was to some degree reduced (although the gradient increased in the flame zone). This related to the large additional fuel and increased local equivalence ratio. The reduction in temperature, albeit not very large, affected the temperature-dependent reactions. It was observed that towards quenching the conversion of H, O and OH was reduced, both for the consumption in the front of the flame and the production in the back. Similarly, the conversion of intermediates CH_3, CH_2O, HCO and HO_2 was reduced (production in front, consumption in the back of the flame). This coincided with less conversion of major species and lesser reaction heat release. Moreover, when observing the individual species balances (CDR budget analysis, Section 3.4), it was seen that the balance of OH was affected earlier than other species. The mass-fraction profiles showed that OH and O (Figs. 9d,f), contrary to other intermediates, were depleted prior to quenching. The large presence of the major reactants CH_4, H_2 and O_2 clearly indicated that the temperature and dilution led to the reduced conversion.

Third, due to the permeation, the gas velocity increased, Fig. 6d, compared to IW. The enhanced convective heat transfer away from the wall and flame contributed to the reduced temperature in the flame. Moreover, a significant amount of unburnt fuel, primarily CO (Fig. 9f), was carried from the flame.

Although not investigated here, except by the limit of no wall mass flux, it could be anticipated that a lower permeation rate should give later quenching and shorter quenching distance. Correspondingly, the initially lean flames also gave lesser quenching distances (Fig. 15).

5. Conclusions

Flame-wall interactions were investigated for a one-dimensional laminar premixed methane-air flame with an isothermal, chemically inert impermeable wall (IW) and a hydrogen-permeable wall (PW). Two temperatures (600 and 750 K) of wall and unburnt gas were selected. Hydrogen released through the permeable wall participated in the methane-air combustion as a secondary fuel.

Initially, it was verified by comparison with GRI 3.0 [37] that for lean and stoichiometric mixtures, the reduced mechanisms of Smooke and Giovangigli [35] (with slightly modified parameters) can represent the chemistry. For rich methane-air mixtures, the DRM22 mechanism [36], including C2-chemistry, can be used. The simulations confirmed previous work on head-on-quenching towards an impermeable wall.

For the permeable wall, the hydrogen flow significantly altered the flame-wall interactions. Flame quenching occurred at a notable distance from the wall. It was apparent that this was neither due to lack of oxidizer nor to heat loss to the wall. Actually, quenching took place before the flame heated the wall significantly. The early quenching appeared to be a result of the mutual effects of large local concentration of H_2, a reduced flame temperature and increased convective heat transfer away from the wall and flame. When the flame approached the wall and the increasing H_2 concentration, OH accumulation was reduced before other species (but O_2) were affected.

Subsequent to quenching, some modest reaction heat release still took place near the wall. This gave a peak wall heat flux a while after the quenching instance, although much less than for the impermeable wall.

The discussion of quenching definitions showed that some are applicable to the PW case. In the present study, the quenching instance was based on the OH gradient [46]. Also definitions based on maximum reaction heat release and of the minimum flame thickness appeared applicable. On the other hand, the definition based on maximum wall heat flux failed to capture the cease of major reaction heat release.

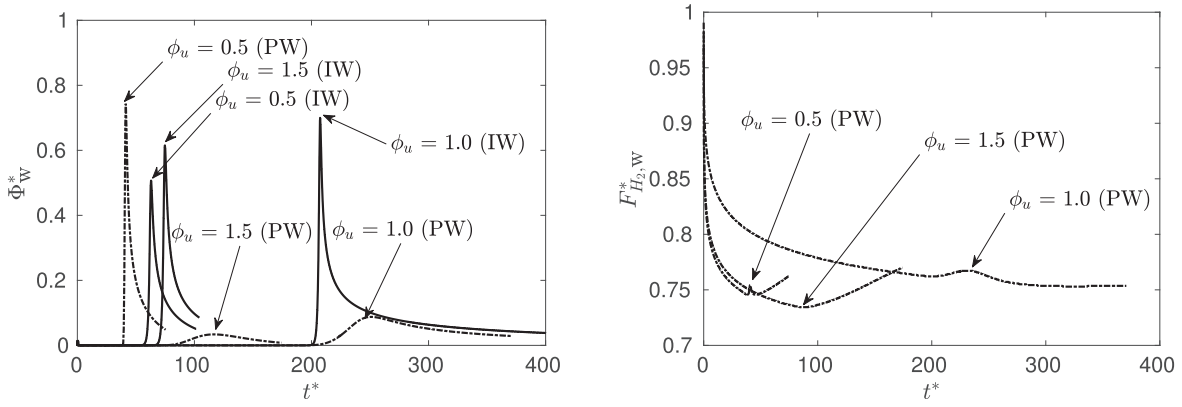

(a) Normalized wall heat fluxes, Φ_w^*. (b) Normalized wall mass fluxes, $F_{H_2,w}^*$.

Fig. 13. Transient wall heat fluxes and mass fluxes for varying ϕ_u for IW and PW at $T_w = 600$ K.

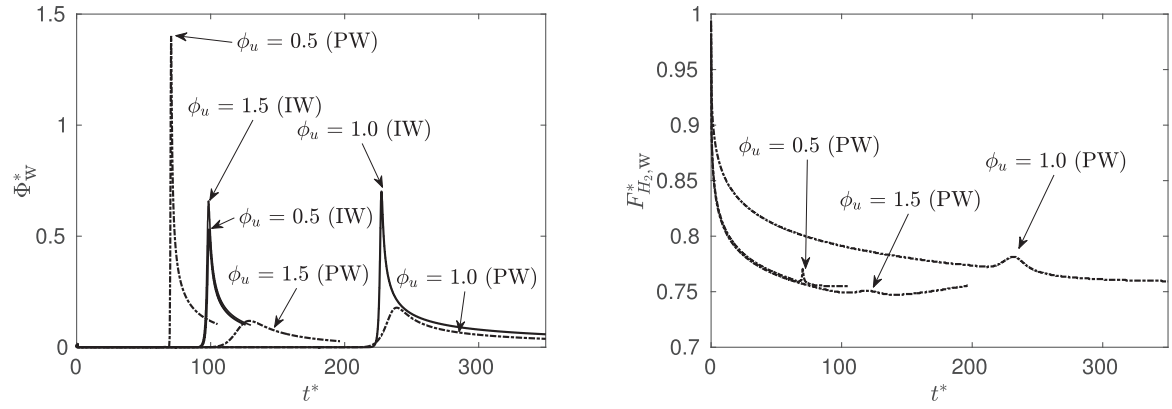

(a) Normalized wall heat fluxes, Φ^*_w. (b) Normalized wall mass fluxes, $F^*_{H_2,w}$.

Fig. 14. Transient wall heat fluxes and mass fluxes for varying ϕ_u for IW and PW at T_w = 750 K.

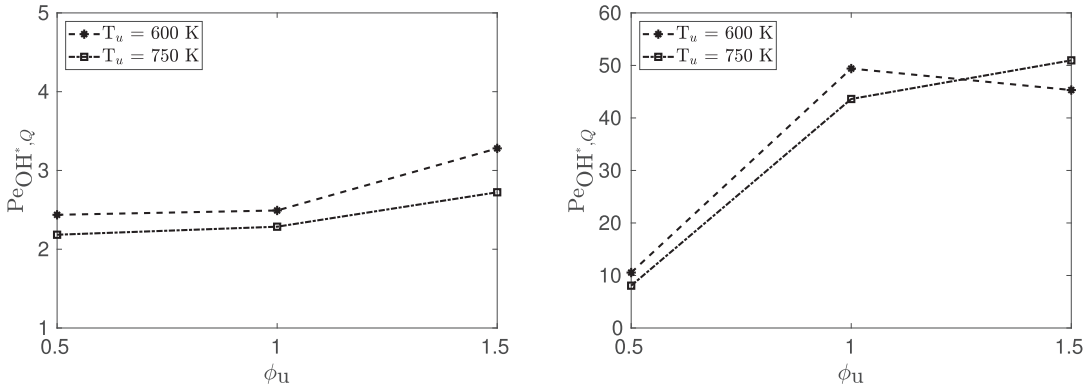

(a) IW (b) PW

Fig. 15. Non-dimensional flame-wall distance at quenching, $Pe_{OH^*,Q}$, for T_w = 600 K and 750 K and varying ϕ_u.

Table 6
Results of various criteria for quenching and the associated flame-wall distances for the case ϕ_u = 1.0 and T_w = 600 K. The criterion for the quenching instance is applied first; then the distance is determined at this instance.

Criterion for quenching		for IW		for PW	
instance, t_Q	distance, y_Q	t^*_Q	y_Q/δ_L	t^*_Q	y_Q/δ_L
OH gradient	max OH gradient	208.5	2.49	168.5	49.4
max Φ_w		207.4		251.0	
	1700 K isocontour		3.5		43.9
	1800 K isocontour		5.2		71.2
	Pe (i.e. max $\dot{\omega}$)		0.0		18.7
	Pe_F (i.e. max $(-\dot{\omega}_F)$)		1.75		20.7
min δ^0_L	δ^0_L	207.4	1.90	161.6	5.43
max $\dot{\omega}$	Pe	207.6	0.0	162.7	57.9
max $(-\dot{\omega}_F)$	Pe_F	203.5	6.40	162.7	57.7
min Pe	Pe	206.9	0.0	245.4	18.4

Declarations of interest

None.

CRediT authorship contribution statement

Prashant S. Salimath: Conceptualization, Software, Validation, Formal analysis, Investigation, Data curation, Writing - original draft, Visualization. **Ivar S. Ertesvåg:** Conceptualization, Formal analysis, Data curation, Writing - original draft, Writing - review & editing, Supervision. **Andrea Gruber:** Conceptualization, Methodology, Software, Data curation, Writing - review & editing, Supervision.

Acknowledgments

The work of the 1st author (Salimath) was partly funded by the Research Council of Norway through the project CCERT – CO2 Capture with Enabling Research and Technology, while the work at SINTEF (Gruber) has been funded by the Research Council of Norway through the project 280578 “Distributed Hydrogen Injection and Combustion Technology for Next Generation Pre-Combustion CCS Schemes”. We are grateful to the Norwegian Metacenter for Computational Science (NOTUR) for providing the HPC computational resources and useful technical support (project No. NN9400K).

References

[1] Poinsot T, Veynante D. Theoretical and numerical combustion. Philadelphia PA, USA: R.T. Edwards Inc; 2005.
[2] Dreizler A, Böhm B. Advanced laser diagnostics for an improved understanding of premixed flame-wall interactions. Proc Combust Inst 2015;35(1):37–64. https://doi.org/10.1016/j.proci.2014.08.014.
[3] Gruber A, Sankaran R, Hawkes E, Chen J. Turbulent flame-wall interaction: a direct numerical simulation study. J Fluid Mech 2010;658:5–32. https://doi.org/10.1017/S0022112010001278.
[4] Gruber A, Salimath PS, Chen JH. Direct numerical simulation of laminar flame-wall interaction for a novel H2-selective membrane/injector configuration. Int J Hydrogen Energy 2014;39(11):5906–18. https://doi.org/10.1016/j.ijhydene.2014.01.148.
[5] Salimath PS, Ertesvåg IS, Gruber A. Premixed hydrogen-air flames interacting with a hydrogen porous wall. Int J Hydrogen Energy 2018;43(7):3822–36. https://doi.org/10.1016/j.ijhydene.2017.12.166.
[6] Westbrook CK, Adamczyk AA, Lavoie GA. A numerical study of laminar flame wall

quenching. Combust Flame 1981;40:81–99. https://doi.org/10.1016/0010-2180(81)90112-7.
[7] Hasse C, Bollig M, Peters N, Dwyer HA. Quenching of laminar iso-octane flames at cold walls. Combust Flame 2000;122(1–2):117–29.
[8] Kiehne TM, Matthews RD, Wilson DE. The significance of intermediate hydrocarbons during wall quench of propane flames. Proc Combust Inst 1986;21(1):481–9. https://doi.org/10.1016/S0082-0784(88)80276-5.
[9] Jiang B, Gordon RL, Talei M. Head-on quenching of laminar premixed methane flames diluted with hot combustion products. Proc Combust Inst 2019;37:5095–103. https://doi.org/10.1016/j.proci.2018.07.120.
[10] Popp P, Baum M. Analysis of wall heat fluxes, reaction mechanisms, and unburnt hydrocarbons during the head-on quenching of a laminar methane flame. Combust Flame 1997;108(3):327–48. https://doi.org/10.1016/S0010-2180(96)00144-7.
[11] Boust B, Sotton J, Labuda SA, Bellenoue M. A thermal formulation for single-wall quenching of transient laminar flames. Combust Flame 2007;149(3):286–94. https://doi.org/10.1016/j.combustflame.2006.12.019.
[12] Owston R, Magi V, Abraham J. A numerical study of thermal and chemical effects in interactions of n-heptane flames with a single surface. Combust Flame 2007;148(3):127–47. https://doi.org/10.1016/j.combustflame.2006.10.006.
[13] Sotton J, Boust B, Labuda SA, Bellenoue M. Head-on quenching of transient laminar flame: heat flux and quenching distance measurements. Combust Sci Technol 2005;177(7):1305–22. https://doi.org/10.1080/00102200590950485.
[14] Ezekoye O, Greif R, Sawyer R. Increased surface temperature effects on wall heat transfer during unsteady flame quenching. Proc Combust Inst 1992;24:1465–72. https://doi.org/10.1016/S0082-0784(06)80171-2.
[15] Popp P, Smooke M, Baum M. Heterogeneous/homogeneous reaction and transport coupling during flame-wall interaction. Proc Combust Inst 1996;26(2):2693–700. https://doi.org/10.1016/S0082-0784(96)80105-6.
[16] Huang W, Vosen S, Greif R. Heat transfer during laminar flame quenching: effect of fuels. Proc Combust Inst 1986;21:1853–60. https://doi.org/10.1016/S0082-0784(88)80420-X.
[17] Dabireau F, Cuenot B, Vermorel O, Poinsot T. Interaction of flames of H2 + O2 with inert walls. Combust Flame 2003;135(1–2):123–33. https://doi.org/10.1016/S0010-2180(03)00000-0.
[18] Mari R, Cuenot B, Rocchi J-P, Selle L, Duchaine F. Effect of pressure on hydrogen/oxygen coupled flame-wall interaction. Combust Flame 2016;168:409–19. https://doi.org/10.1016/j.combustflame.2016.01.004.
[19] Owston R, Magi V, Abraham J. Interactions of hydrogen flames with walls: Influence of wall temperature, pressure, equivalence ratio, and diluents. Int J Hydrogen Energy 2007;32(12):2094–104. https://doi.org/10.1016/j.ijhydene.2006.07.030.
[20] Aghalayam P, Bui PA, Vlachos DG. The role of radical wall quenching in flame stability and wall heat flux: hydrogen-air mixtures. Combust Theory Model 1998;2(4):515–30. https://doi.org/10.1088/1364-7830/2/4/010.
[21] Yenerdag B, Minamoto Y, Aoki K, Shimura M, Nada Y, Tanahashi M. Flame-wall interactions of lean premixed flames under elevated, rising pressure conditions. Fuel 2017;189:8–14. https://doi.org/10.1016/j.fuel.2016.10.096.
[22] Vosen S, Greif R, Westbrook C. Unsteady heat transfer during laminar flame quenching. Proc Combust Inst 1984;20:75–83. https://doi.org/10.1016/S0082-0784(85)80490-2.
[23] Ghani A, Poinsot T. Flame quenching at walls: a source of sound generation. Flow, Turbul Combust 2017;99(1):173–84. https://doi.org/10.1007/s10494-017-9810-5.
[24] Gounder JD, Kutne P, Gruber A. Experimental Investigation of a Bluff Body Burner for Distributed Hydrogen Injection. In: GT2017, Volume 4A: Combustion, Fuels and Emissions, ISBN 978-0-7918-5084-8; 2017.https://doi.org/10.1115/GT2017-63414.
[25] Chen J, Choudhary A, de Supinski B, DeVries M, Hawkes E, Klasky S, Liao W, Ma K, Mellor-Crummey J, Podhorszki N, Sankaran R, Shende S, Yoo C. Terascale direct numerical simulations of turbulent combustion using S3D. Comput Sci Discov 2009;2(1):15001. https://doi.org/10.1088/1749-4699/2/1/015001.
[26] Chen J. Petascale direct numerical simulation of turbulent combustion – fundamental insights towards predictive models. Proc Combust Inst 2011;33(1):99–123. https://doi.org/10.1016/j.proci.2010.09.012.
[27] Sankaran R, Hawkes E, Chen J, Lu T, Law C. Direct numerical simulations of turbulent lean premixed combustion. J Phys Conf Ser 2006;46(1):38–42. https://doi.org/10.1088/1742-6596/46/1/004.
[28] Grout RW, Gruber A, Yoo CS, Chen JH. Direct numerical simulation of flame stabilization downstream of a transverse fuel jet in cross-flow. Proc Combust Inst 2011;33(1):1629–37. https://doi.org/10.1016/j.proci.2010.06.013.
[29] Hawkes E, Sankaran R, Sutherland J, Chen J. Scalar mixing in direct numerical simulations of temporally evolving plane jet flames with skeletal CO/H2 kinetics. Proc Combust Inst 2007;31(1):1633–40. https://doi.org/10.1016/j.proci.2006.08.079.
[30] Lignell DO, Chen JH, Smith PJ, Lu T, Law CK. The effect of flame structure on soot formation and transport in turbulent nonpremixed flames using direct numerical simulation. Combust Flame 2007;151(1–2):2–28. https://doi.org/10.1016/j.combustflame.2007.05.013.
[31] Sankaran R, Im HG, Hawkes ER, Chen JH. The effects of non-uniform temperature distribution on the ignition of a lean homogeneous hydrogen-air mixture. Proc Combust Inst 2005;30(1):875–82. https://doi.org/10.1016/j.proci.2004.08.176.
[32] Echekki T, Chen JH. Direct numerical simulation of autoignition in non-homogenous hydrogen-air mixtures. Combust Flame 2003;134(3):169–91. https://doi.org/10.1016/S0010-2180(03)00088-9.
[33] Kennedy CA, Carpenter MH. Several new numerical methods for compressible shear-layer simulations. Appl Numer Math 1994;14(804):397–433. https://doi.org/10.1016/0168-9274(94)00004-2.
[34] Ganter S, Heinrich A, Meier T, Kuenne G, Jainski C, Rißmann MC, Dreizler A, Janicka J. Numerical analysis of laminar methane-air side-wall-quenching. Combust Flame 2017;186:299–310. https://doi.org/10.1016/j.combustflame.2017.08.017.
[35] Smooke M, Giovangigli V. Formulation of the premixed and nonpremixed test problems. In: Smooke M, editor. Lect. Notes Phys. vol. 384. Springer Verlag; 1991. p. 1–28.
[36] Kazakov A, Frenklach M. Reduced Reaction Sets Based on GRI-Mech 1.2. URL: combustion.berkeley.edu/drm [accessed 19 Nov. 2019].
[37] Smith GP, Golden DM, Frenklach M, Eiteener B, Goldenberg M, Bowman CT, Hanson RK, Song S, Gardiner WC, Lissianski VV, Qin Z. GRI-Mech 3.0. URL: combustion.berkeley.edu/gri_mech/ [accessed 22 Nov. 2019].
[38] Kee RJ, Rupley FM, Miller JA. CHEMKIN-II: A FORTRAN chemical kinetics package for the analysis of gas phase chemical kinetics, SANDIA Rep. No. SAND89-8009B; 1989, pp. 3–164.
[39] Kee RJ, Dixon LG, Warnatz J, Coltrin ME, Miller JA, Moffat HK. A fortran chemical kinetics package for the analysis of gas-phase chemical kinetics [Tech. Rep.]. Release 3.5. Reaction Design Inc.: San Diego, CA; 1999.
[40] Bredesen R, Jordal K, Bolland O. High-temperature membranes in power generation with CO2 capture. Chem Eng Process Process Intensif 2004;43(9):1129–58. https://doi.org/10.1016/j.cep.2003.11.011.
[41] Gustafsson B, Sundström A. Incompletely parabolic problems in fluid dynamics. SIAM J Appl Math 1978;35(2):343–57. https://doi.org/10.1137/0135030.
[42] Nordström J, Svärd M. Well-posed boundary conditions for the Navier-Stokes equations. SIAM J Numer Anal 2005;43(3):1231–55. https://doi.org/10.1137/040604972.
[43] Strikwerda JC. Initial boundary value problems for incompletely parabolic systems. Commun Pure Appl Math 1977;30(6):797–822. https://doi.org/10.1002/cpa.3160300606.
[44] Yoo CS, Wang Y, Trouvé A, Im HG. Characteristic boundary conditions for direct simulations of turbulent counterflow flames. Combust Theory Model 2005;9(1):617–46. https://doi.org/10.1080/13647830500307378.
[45] Yoo CS, Im HG. Characteristic boundary conditions for simulations of compressible reacting flows with multi-dimensional, viscous and reaction effects. Combust Theory Model 2007;11(2):259–86. https://doi.org/10.1080/13647830600898995.
[46] Jainski C, Rißmann M, Böhm B, Janicka J, Dreizler A. Sidewall quenching of atmospheric laminar premixed flames studied by laser-based diagnostics. Combust Flame 2017;183:271–82. https://doi.org/10.1016/j.combustflame.2017.05.020.
[47] Jainski C, Rißmann M, Böhm B, Dreizler A. Experimental investigation of flame surface density and mean reaction rate during flame-wall interaction. Proc Combust Inst 2017;36(2):1827–34. https://doi.org/10.1016/j.proci.2016.07.113.
[48] Poinsot T, Haworth DC, Bruneaux G. Direct simulation and modeling of flame-wall interaction for premixed turbulent combustion. Combust Flame 1993;95(1–2):118–32. https://doi.org/10.1016/0010-2180(93)90056-9.
[49] Barlow R, Smith N, Chen J-Y, Bilger R. Nitric oxide formation in dilute hydrogen jet flames: isolation of the effects of radiation and turbulence-chemistry submodels. Combust Flame 1999;117(1):4–31. https://doi.org/10.1016/S0010-2180(98)00071-6.
[50] Radiation models URL: www.sandia.gov/TNF/radiation.html (accessed 20 June 2019).